

RESEARCH ARTICLE

[View Article Online](#)
[View Journal](#) | [View Issue](#)



Cite this: *Inorg. Chem. Front.*, 2024, **11**, 2681

Pb_{3.5}GeS₄Br₃: the first phase-matching thiogermanate halide infrared nonlinear optical material†

Jiazheng Zhou,‡^{a,b} Hongshan Wang,‡^b Junjie Liu,‡^a Xin Su, Yu Chu, Jiale Qu*^a and Xiangzhan Jiang*^a

Two new thiohalides Pb₃GeS₄Br₂ and Pb_{3.5}GeS₄Br₃ have been synthesized by introducing Pb²⁺ into the thiogermanate system. The compounds crystallize in centrosymmetric *P*2₁/*c* (Pb₃GeS₄Br₂) and non-centrosymmetric *P*6₃ (Pb_{3.5}GeS₄Br₃) space groups, respectively. To the best of our knowledge, Pb₃GeS₄Br₂ and Pb_{3.5}GeS₄Br₃ are the first Pb-containing thiogermanate halides, and the latter is the first phase-matching IR nonlinear optical material in the thiogermanate halide system. Due to the presence of Pb²⁺ with stereochemically active lone pair electrons, Pb₃GeS₄Br₂ exhibits a strong optical anisotropy with a birefringence of 0.131@1064 nm, while Pb_{3.5}GeS₄Br₃ shows a large second-harmonic generation response (0.8 × AgGaS₂) and high laser-induced damage threshold (3.0 × AgGaS₂). These results enrich the structural and chemical diversity of chalcohalides.

Received 30th January 2024,
Accepted 22nd March 2024
DOI: 10.1039/d4qi00293h
rsc.li/frontiers-inorganic

Introduction

As a key device for frequency conversion in all-solid-state lasers, nonlinear optical (NLO) materials are widely applied in many fields, such as spectroscopic technology, laser photolithography, photomedicine, environmental monitoring, and so on.^{1–6} Based on their operating regions, NLO materials can be classified into deep-ultraviolet (DUV), ultraviolet-visible to near-infrared (UV-vis-NIR), and mid- to far-infrared (IR) NLO materials. In the past few decades, a large number of excellent oxide-based UV or DUV NLO materials, including β -Ba₂O₄,⁷ LiB₃O₅,⁸ KH₂PO₄,⁹ KTiOPO₄,^{10,11} KBe₂BO₃F₂,¹² and NH₄B₄O₆F,¹³ have been rationally designed and fabricated,^{14–17} while for mid- and far-IR bands, the commercialized NLO materials are composed of chalcopyrite-like AgGaS₂ (AGS), AgGaSe₂ (AGSe) and ZnGeP₂ (ZGP).^{18–20} Nevertheless, due to the intrinsic drawbacks of these materials, such as the low laser-induced damage threshold (LIDT) in AGS and AGSe,²¹ the non-phase matching behavior of AGSe and strong two-photon absorption in ZGP at around \sim 1 μ m, their applications

are highly limited. Therefore, it is necessary to develop new IR NLO materials with high performance.^{22–24}

In general, an excellent IR NLO material should meet the following requirements: (1) large second-harmonic generation (SHG) response $\geq 0.5 \times$ AGS, preferably $\geq 1.0 \times$ AGS; (2) high LIDT $\geq 2.0 \times$ AGS for high-power laser output; (3) wide optical transparent range that covers the two important atmospheric windows, 3–5 and/or 8–12 μ m; (4) suitable birefringence (> 0.03) to achieve phase matching (PM), which is critical for the practical application of NLO materials; (5) good crystal growth habits and thermal stability.^{25–33} However, it is challenging to satisfy these requirements in one compound. To explore new IR NLO materials, metal chalcohalides have received considerable attention due to their abundant structural diversity and adjustable optical properties.^{34–36} Meanwhile, chalcohalides are expected to inherit the intrinsic advantages of both chalcogenides and halides. Recent results indicate that the salt-inclusion framework can effectively improve the optical band gap of chalcohalides,^{37–39} resulting in balanced optical properties among these compounds. Hence, the salt-inclusion chalcogenides (SICs) have emerged as promising systems for the exploration of new IR NLO materials,^{40–42} and a series of new SICs has been developed. It is worth noting that 9 compounds, [Ba₄Cl₂][Ge₃Se₉], [Ba₄Br₂][Ge₃Se₉], [Ba₄Cl₂][Ge₃S₉], [KS₄Cl][Ge₃S₁₀], [NaSr₄Cl][Ge₃S₁₀], [KBa₄Cl][Ge₃S₁₀], [Sr₄Cl₂][Ge₃S₉], [NaBa₄Cl][Ge₃S₁₀], and [K₂Ba₃Cl₂][Ge₃S₉], have been reported with the thiogermanate halide system. Despite showing evident SHG responses, none of them possesses PM behavior,^{43–48} which can be attributed to the small birefringence in these compounds.

^aInstitute of Rehabilitation Engineering, Binzhou Medical University, Yantai, 264003, China. E-mail: qujiale@buaa.edu.cn, xzjiang@bzm.edu.cn

^bResearch Center for Crystal Materials, State Key Laboratory of Functional Materials and Devices for Special Environmental Conditions, Xinjiang Key Laboratory of Functional Crystal Materials, Xinjiang Technical Institute of Physics & Chemistry, CAS, 40-1 South Beijing Road, Urumqi 830011, China. E-mail: chuy@ms.xjb.ac.cn

† Electronic supplementary information (ESI) available. CCDC 2329605 and 2329606. For ESI and crystallographic data in CIF or other electronic format see DOI: <https://doi.org/10.1039/d4qi00293h>

‡ These authors contributed equally to this work.

To increase the optical anisotropy and birefringence, introducing Pb^{2+} , Sb^{3+} , and Sn^{2+} cations with stereochemically active lone pair (SCALP) electrons into the structure has been demonstrated as a feasible strategy.⁴⁹ In this work, by introducing Pb^{2+} into thiogermanate halides, the first Pb-containing thiogermanate halides, $\text{Pb}_3\text{GeS}_4\text{Br}_2$ and $\text{Pb}_{3.5}\text{GeS}_4\text{Br}_3$, have been rationally designed and fabricated by a high-temperature solution method. $\text{Pb}_3\text{GeS}_4\text{Br}_2$ crystallizes in the centrosymmetric (CS) $P2_1/c$ space group and is composed of $[\text{PbS}_4\text{Br}_4]$, $[\text{PbS}_3\text{Br}_3]$, $[\text{PbS}_8]$ and $[\text{GeS}_4]$ units. It exhibits strong optical anisotropy and a large birefringence of 0.131@1064 nm due to the presence of Pb^{2+} with SCALP electrons. While $\text{Pb}_{3.5}\text{GeS}_4\text{Br}_3$ crystallizes in the non-centrosymmetric (NCS) $P6_3$ space group and is built from $[\text{PbS}_4\text{Br}_4]$, $[\text{PbBr}_6]$ and $[\text{GeS}_4]$ units. Based on statistical analyses, $\text{Pb}_{3.5}\text{GeS}_4\text{Br}_3$ is the first thiogermanate halide IR NLO material with PM behavior. This compound shows a strong SHG response of $0.8 \times \text{AGS}$ and has a high LIDT of $3 \times \text{AGS}$.

Experimental procedures

Reagents and syntheses

The raw reagents of PbBr_2 ($\geq 99\%$), Ge ($\geq 99.99\%$), and S ($\geq 99.99\%$) were commercially purchased from Aladdin Industrial Inc. The small single crystals of $\text{Pb}_3\text{GeS}_4\text{Br}_2$ and $\text{Pb}_{3.5}\text{GeS}_4\text{Br}_3$ for structural determinations were prepared by the high-temperature solution method. The starting materials of PbBr_2 , Ge and S were weighed and loaded into graphite crucibles with the ratio of 3:1:4 ($\text{Pb}_3\text{GeS}_4\text{Br}_2$) and 3.5:1:4 ($\text{Pb}_{3.5}\text{GeS}_4\text{Br}_3$), and then placed in silica tubes. The tubes were further sealed with methane–oxygen flame under a high vacuum of 10^{-3} Pa. After that, the sealed tubes were placed into a computer-controlled furnace and the heating program was set to 650 °C ($\text{Pb}_3\text{GeS}_4\text{Br}_2$) in 30 h, and 600 °C ($\text{Pb}_{3.5}\text{GeS}_4\text{Br}_3$) in 28 h, kept at that temperature for 48 h, and then cooled to room temperature at a rate of 1 °C h⁻¹. Finally, small orange single crystals of $\text{Pb}_3\text{GeS}_4\text{Br}_2$ and $\text{Pb}_{3.5}\text{GeS}_4\text{Br}_3$ (Fig. S1†) were harvested.

Single-crystal X-ray diffraction (SC-XRD)

A Bruker SMART APEX II CCD single-crystal X-ray diffractometer using graphite-monochromatized molybdenum $\text{K}\alpha$ radiation ($\lambda = 0.71073$ Å) was utilized to collect the crystal data at 273 K. High-quality single crystals were selected under an optical microscope for collecting the X-ray diffraction data. The SADABS program⁵⁰ was used to perform the multiscan-type absorption correction. Then the XPREP program in the SHELX program package was used to determine the space group, and the SHELXT and XL programs⁵¹ were applied to solve and refine the structure data by direct methods and full-matrix least-squares on F^2 . Finally, the PLATON program⁵² was used to check the possible missing symmetry elements, and no higher symmetry was found.

Powder XRD

A Bruker D2 PHASER diffractometer with Cu $\text{K}\alpha$ radiation ($\lambda = 1.5418$ Å) was utilized to record the powder XRD patterns. The

collected 2θ range was set to 10–70° with a scan rate of 0.02° s⁻¹. The theoretical patterns of the compounds were obtained by Mercury software based on the CIF file of $\text{Pb}_3\text{GeS}_4\text{Br}_2$ and $\text{Pb}_{3.5}\text{GeS}_4\text{Br}_3$.

Energy-dispersive X-ray spectroscopy (EDS)

The EDS spectrum and mapping of the title compounds were characterized on a field emission scanning electron microscope (FE-SEM, JEOL JSM-7610F Plus, Japan) equipped with an energy-dispersive X-ray spectrometer (Oxford, X-Max 50), which was operated at 5 kV. The measurements were carried out on the small single crystals of $\text{Pb}_3\text{GeS}_4\text{Br}_2$ and $\text{Pb}_{3.5}\text{GeS}_4\text{Br}_3$. The EDS spectra and mappings confirm the presence of Pb, Ge, S and Br elements in the both compounds (Fig. S2a†).

Raman spectroscopy

The Raman spectra of $\text{Pb}_3\text{GeS}_4\text{Br}_2$ and $\text{Pb}_{3.5}\text{GeS}_4\text{Br}_3$ were recorded on a LABRAM HR evolution spectrometer equipped with a CCD detector using 532 nm radiation. The Raman spectra were collected in the 4000–100 cm⁻¹ region.

UV-vis-NIR diffuse-reflectance spectroscopy

A SolidSpec-3700 DUV spectrophotometer was used to determine the UV-vis-NIR diffuse-reflectance spectra of pure phase $\text{Pb}_{3.5}\text{GeS}_4\text{Br}_3$ powder samples at room temperature. The measured wavelength range is 200–2600 nm. To figure out the experimental band gap, the collected data were converted to absorbance by the Kubelka–Munk function⁵³ $F(R) = \alpha/S = (1 - R)^2/2R$, where $F(R)$ is the ratio of the absorption coefficient to scattering coefficient; α is the absorption coefficient; R is the reflectance; and S is the scattering coefficient.

Refractive index difference (RID) value measurement

The RID of $\text{Pb}_{3.5}\text{GeS}_4\text{Br}_3$ was measured on a polarizing microscope (ZEISS Axio Scope.5 Pol) equipped with a Berek compensator. The wavelength of the light source was 546 nm. The difference in the optical path (D) for one direction was determined according to the interference color with the maximum value of the crystal under polarized light. The RID can be calculated using eqn (1):

$$D = |N_2 - N_1| \times T = \Delta n \times T \quad (1)$$

where Δn denotes the difference in the refractive index and T denotes the thickness of the crystal.

Theoretical calculations

The band structure, total/partial density of states, and optical properties of $\text{Pb}_3\text{GeS}_4\text{Br}_2$ were calculated by using the plane-wave pseudopotential method implemented in the CASTEP based on the density functional theory (DFT) method.⁵⁴ Perdew–Burke–Ernzerhof (PBE) exchange–correlation of generalized gradient approximation (GGA)^{55,56} was applied in the calculations. The interactions between the core and electrons were described by the norm-conserving pseudopotential

(NCP).⁵⁷ The Monkhorst–Pack scheme was set as 0.03 Å. The valence electrons were set as Pb 5d¹⁰ 6s² 6p², Ge 4s² 4p², S 3s² 3p⁴ and Br 4s² 4p⁵. The kinetic energy cutoffs were set to be 820 eV. The Heyd–Scuseria–Ernzerhof 06 (HSE06) hybrid functional⁵⁸ was performed using the PWmat code, which runs on graphics processing unit (GPU) processors. The pseudo-potential NCPP-SG15-PBE and 50 Ryd plane wave cut-off energy were used in the calculations:

$$E_{\text{XC}}^{\text{HSE}} = \alpha E_{\text{X}}^{\text{HF,SR}}(\mu) + (1 - \alpha) E_{\text{X}}^{\text{PBE,SR}}(\mu) + E_{\text{X}}^{\text{PBE,LR}}(\mu) + E_{\text{C}}^{\text{PBE}} \quad (2)$$

where α is the mixing parameter; μ is the adjustable parameter controlling the short-range interaction; $E_{\text{X}}^{\text{HF,SR}}(\mu)$ is the short-range Hartree–Fock exact exchange functional; $E_{\text{X}}^{\text{PBE,SR}}(\mu)$ and $E_{\text{X}}^{\text{PBE,LR}}(\mu)$ are the short- and long-range components of the PBE exchange functional; and $E_{\text{C}}^{\text{PBE}}$ is the PBE correlation functional. In HSE06, the parameters are suggested as $\alpha = 0.25$.

LIDT measurements

The resistance to laser damage of $\text{Pb}_{3.5}\text{GeS}_4\text{Br}_3$ was evaluated by a single-pulse LIDT method with an incident laser at 1064 nm (10 ns, 10 Hz). Micro-crystal samples of $\text{Pb}_{3.5}\text{GeS}_4\text{Br}_3$ with the particle size range $\leq 45 \mu\text{m}$ were applied for the measurements, and AGS samples with the same sizes were used as the reference. The laser directly irradiated the samples. The output energy of the laser was increased until the samples were damaged. The color change of the samples was carefully observed under an optical microscope. The damage energies were measured to $\sim 0.12 \mu\text{J}$ for $\text{Pb}_{3.5}\text{GeS}_4\text{Br}_3$, and $\sim 0.04 \mu\text{J}$ for AGS. The LIDT of $\text{Pb}_{3.5}\text{GeS}_4\text{Br}_3$ was calculated to be $\sim 3 \times \text{AGS}$ from the following formula (3):

$$\text{LIDT}(\text{Pb}_{3.5}\text{GeS}_4\text{Br}_3) = \text{LIDT}(\text{AGS}) \times \frac{I(\text{Pb}_{3.5}\text{GeS}_4\text{Br}_3)}{I(\text{AGS})} \cong 3 \times \text{AGS} \quad (3)$$

where I is the laser damage energy of a single pulse.

Second-harmonic generation measurements

The SHG responses of $\text{Pb}_{3.5}\text{GeS}_4\text{Br}_3$ were evaluated by the Kurtz–Perry method,⁵⁹ and AGS was used as the reference. The powder samples of $\text{Pb}_{3.5}\text{GeS}_4\text{Br}_3$ and AGS were ground and sieved into distinct particle size ranges (≤ 45 , 45–63, 63–90, 90–125, 125–180 and 180–212 μm). The experiments were carried out using a 2.09 μm Q-switch laser. The SHG signals were detected by a photomultiplier tube and recorded on an oscilloscope.

Results and discussion

The $\text{Pb}_3\text{GeS}_4\text{Br}_2$ and $\text{Pb}_{3.5}\text{GeS}_4\text{Br}_3$ single crystals for structural determination were fabricated by the high-temperature solution method in a sealed carbon crucible. To avoid high vapour pressure-induced experimental failures, a slow heating rate

from room temperature to 650 °C ($\text{Pb}_3\text{GeS}_4\text{Br}_2$) or 600 °C ($\text{Pb}_{3.5}\text{GeS}_4\text{Br}_3$) was utilized (for the detailed experimental process, see the Experimental sections). The results of SC-XRD show that $\text{Pb}_3\text{GeS}_4\text{Br}_2$ crystallizes in the monoclinic system with the $P2_1/c$ space group, with cell parameters $a = 12.8452(9)$ Å, $b = 8.0502(5)$ Å, $c = 11.4712(8)$ Å, $\beta = 116.129(2)^\circ$ and $Z = 4$. $\text{Pb}_{3.5}\text{GeS}_4\text{Br}_3$ crystallizes in the hexagonal system with the $P6_3$ space group, with cell parameters $a = b = 11.0145(2)$ Å, $c = 6.0539(2)$ Å, and $Z = 2$. The crystal data and structure refinement information, including the atomic coordinates and equivalent isotropic displacement parameters, bond lengths and angles information, are given in the ESI† (Tables 1 and S1–S8†).

In $\text{Pb}_3\text{GeS}_4\text{Br}_2$, there are three crystallographically unique Pb atoms, one Ge atom, four S atoms and two Br atoms in its asymmetric unit. Pb1, Pb2, and Pb3 atoms are coordinated with S and Br atoms to form $[\text{Pb}_1\text{S}_4\text{Br}_4]$, $[\text{Pb}_2\text{S}_3\text{Br}_3]$ and $[\text{Pb}_3\text{S}_8]$ units, with bond lengths $d_{\text{Pb–S}} = 2.760\text{–}3.601$ Å and $d_{\text{Pb–Br}} = 2.843\text{–}3.669$ Å. The Ge atom is connected with four S atoms to

Table 1 Crystal data and structure refinements of $\text{Pb}_3\text{GeS}_4\text{Br}_2$ and $\text{Pb}_{3.5}\text{GeS}_4\text{Br}_3$

| Empirical formula | $\text{Pb}_3\text{GeS}_4\text{Br}_2$ | $\text{Pb}_{3.5}\text{GeS}_4\text{Br}_3$ |
|---|---|--|
| Formula weight (Da) | 982.22 | 1165.73 |
| Temperature (K) | 273.15 | 273.15 |
| Crystal system, space group | Monoclinic, $P2_1/c$ | Hexagonal, $P6_3$ |
| Unit cell dimensions (Å) | $a = 12.8452(9)$ $b = 8.0502(5)$ $c = 11.4712(8)$ $\beta = 116.129(2)^\circ$ | $a = b = 11.0145(2)$ $c = 6.0539(2)$ |
| Volume (Å ³) | 1064.97(13) | 636.06(3) |
| Z | 4 | 2 |
| Calculated density (Mg m ⁻³) | 6.126 | 6.087 |
| Completeness (%) | 99 | 97 |
| Absorption coefficient (mm ⁻¹) | 58.296 | 58.535 |
| $F(000)$ | 1648.0 | 976.0 |
| 2 θ range for data collection/° | 3.532 to 55.026 | 4.27 to 50.578 |
| Index ranges | $-16 \leq h \leq 16$, $-10 \leq k \leq 10$, $-14 \leq l \leq 14$ | $-13 \leq h \leq 13$, $-13 \leq k \leq 13$, $-7 \leq l \leq 7$ |
| Reflections collected | 12 072 | 8186 |
| Independent reflections | 2426 [$R_{\text{int}} = 0.0780$, $R_{\text{sigma}} = 0.0593$] | 751 [$R_{\text{int}} = 0.0516$, $R_{\text{sigma}} = 0.0300$] |
| Observed reflections | 2269 | 743 |
| $[I > 2\sigma(I)]$ | | |
| Data/restraints/parameters | 2426/0/91 | 751/1/38 |
| Absorption correction type | Multi-scan | Multi-scan |
| Goodness-of-fit on F^2 | 1.079 | 1.014 |
| Final R indices ($F_{\text{o}}^2 > 2\sigma(F_{\text{o}}^2)$) ^a | $R_1 = 0.0372$, $wR_2 = 0.0853$ | $R_1 = 0.0136$, $wR_2 = 0.0311$ |
| R indices (all data) ^a | $R_1 = 0.0395$, $wR_2 = 0.0869$ | $R_1 = 0.0140$, $wR_2 = 0.0312$ |
| Largest diff. peak and hole (e Å ⁻³) | 3.48 and -2.10 | 0.47 and -0.5 |
| Flack parameter | — | 0.023(8) |

^a $R_1 = \sum ||F_{\text{o}}|| - |F_{\text{c}}|| / \sum |F_{\text{o}}|$ and $wR_2 = [\sum w(F_{\text{o}}^2 - F_{\text{c}}^2)^2 / \sum wF_{\text{o}}^4]^{1/2}$ for $F_{\text{o}}^2 > 2\sigma(F_{\text{o}}^2)$.

form isolated $[\text{GeS}_4]$ tetrahedral units with $d_{\text{Ge-S}} = 2.193\text{--}2.218 \text{ \AA}$ (Fig. 1a). To further check the formed $[\text{Pb}_1\text{S}_4\text{Br}_4]$, $[\text{Pb}_2\text{S}_3\text{Br}_3]$, $[\text{Pb}_3\text{S}_8]$ and $[\text{GeS}_4]$ units, the Raman spectra of the title compounds were investigated. As shown in Fig. S2b,[†] according to previous studies, the characteristic peaks of the $[\text{GeS}_4]$ tetrahedral unit are located at ~ 234 and $\sim 358 \text{ cm}^{-1}$.^{46,60} The characteristic peaks of the Pb–Br bond are located at ~ 61 and $\sim 134 \text{ cm}^{-1}$,⁶¹ and the peaks at ~ 200 and $\sim 394 \text{ cm}^{-1}$ can be ascribed to the vibrations of Pb–S bonds.⁶² The formed $[\text{Pb}_1\text{S}_4\text{Br}_4]$, $[\text{Pb}_2\text{S}_3\text{Br}_3]$ and $[\text{Pb}_3\text{S}_8]$ groups are linked with each other to build a three-dimensional (3D) $[\text{Pb}_3\text{S}_{12}\text{Br}_7]$ framework (Fig. 1b). The $[\text{GeS}_4]$ tetrahedral units form a $[\text{GeS}_4]$ pseudo-layer structure along the a axis (Fig. 1c). The $[\text{GeS}_4]$ units are placed in the $[\text{Pb}_3\text{S}_{12}\text{Br}_7]$ framework by sharing S atoms to result in the final 3D crystal structure of $\text{Pb}_3\text{GeS}_4\text{Br}_2$ (Fig. 1d).

$\text{Pb}_{3.5}\text{GeS}_4\text{Br}_3$ crystallizes in the hexagonal system with the $P6_3$ space group. There are two crystallographically unique Pb atoms, one Ge atom, two S atoms and one Br atom in its asymmetric unit. The Pb1 atom is coordinated with four S atoms and four Br atoms to construct $[\text{Pb}_1\text{S}_4\text{Br}_4]$ units with $d_{\text{Pb-S}} = 2.779\text{--}3.274 \text{ \AA}$ and $d_{\text{Pb-Br}} = 3.203\text{--}3.598 \text{ \AA}$. It is worth noting that the Pb2 atom is half-occupied and coordinated with four Br atoms to form a $[\text{Pb}_2\text{Br}_6]$ octahedron with $d_{\text{Pb-Br}} = 2.961\text{--}2.970 \text{ \AA}$. The Ge atom is connected with four S atoms to form isolated $[\text{GeS}_4]$ tetrahedral units with $d_{\text{Ge-S}} = 2.191\text{--}2.225 \text{ \AA}$ (Fig. 2a). Similarly, the Raman peaks at ~ 252 and $\sim 363 \text{ cm}^{-1}$ can be attributed to the vibrations of the $[\text{GeS}_4]$ tetrahedral unit,^{46,60} while the peaks at ~ 61 and $\sim 134 \text{ cm}^{-1}$ can be attributed to the vibrations of Pb–Br bonds,⁶¹ and the peaks at ~ 200 and $\sim 397 \text{ cm}^{-1}$ can be attributed to the vibrations of Pb–S bonds,⁶² confirming the chemical bonding in the structure (Fig. S2b[†]). The formed $[\text{Pb}_1\text{S}_4\text{Br}_4]$ units are further connected to each other by sharing S and Br

atoms to build a tunnel-like three-dimensional (3D) $[\text{Pb}_6\text{S}_{21}\text{Br}_{12}]_n$ framework (Fig. 2b). Each $[\text{Pb}_2\text{Br}_6]$ octahedron face shares three Br atoms along the c axis to form one-dimensional (1D) $[\text{Pb}_2\text{Br}_3]_n$ chains (Fig. 2c). The isolated $[\text{GeS}_4]$ tetrahedral units spiral around the $[\text{Pb}_2\text{Br}_3]_n$ chains along the c axis (Fig. 2d) to form a $[\text{GeS}_4]$ tunnel-like 0D framework (Fig. 2e). The Pb1 atoms and $[\text{Pb}_2\text{Br}_3]_n$ 1D chains located within the $[\text{GeS}_4]$ framework form the final 3D structure (Fig. 2e and f).

To clearly show the structural difference, a detailed structural comparison between the two compounds was carried out. It is worth noting that the $[\text{GeS}_4]$ tetrahedra are isolated in both compounds. However, in $\text{Pb}_3\text{GeS}_4\text{Br}_2$, the $[\text{GeS}_4]$ tetrahedra are located in the glide plane with antiparallel orientation (Fig. S3a[†]). Accompanied by an increase in the Pb and Br ratios in $\text{Pb}_{3.5}\text{GeS}_4\text{Br}_3$ (Fig. S3c[†]), the $[\text{GeS}_4]$ tetrahedra are arranged around a columnar configuration formed by the $[\text{Pb}_2\text{Br}_6]$ octahedron, showing a more consistent orientation. Moreover, in $[\text{Pb}_3\text{GeS}_4\text{Br}_2]$, the $[\text{Pb}_2\text{S}_3\text{Br}_3]$ units show an umbrella-like morphology, indicating that the Pb^{2+} ion has a strong lone pair effect; meanwhile, in $\text{Pb}_{3.5}\text{GeS}_4\text{Br}_3$, ball-shaped units $[\text{Pb}_1\text{S}_4\text{Br}_4]$ without lone pair electrons are observed.

To evaluate the optical properties of the title compounds, the syntheses of pure phase powder samples were attempted. $\text{Pb}_{3.5}\text{GeS}_4\text{Br}_3$ powder samples were synthesized at $550 \text{ }^\circ\text{C}$ with a starting mixture of $\text{PbBr}_2 : \text{Ge} : \text{S} = 3.5 : 1 : 4$. The experimental powder XRD patterns indicate that the main phase of the synthesized polycrystalline powder samples is noncentrosymmetric $\text{Pb}_{3.5}\text{GeS}_4\text{Br}_3$. However, there is a small amount of the centrosymmetric $\text{Pb}_3\text{GeS}_4\text{Br}_2$ secondary phase in the samples (Fig. S4a[†]), confirming the purity of $\text{Pb}_{3.5}\text{GeS}_4\text{Br}_3$. The synthesis of $\text{Pb}_3\text{GeS}_4\text{Br}_2$ polycrystalline samples was carried out at different temperatures (500 , 600 and $700 \text{ }^\circ\text{C}$) with diverse start-

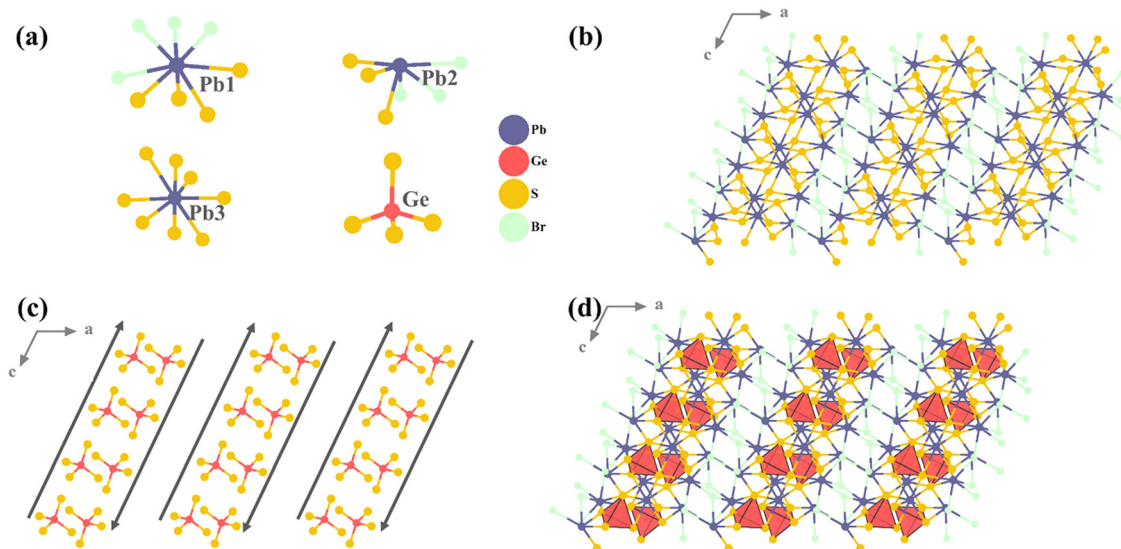


Fig. 1 Crystal structure of $\text{Pb}_3\text{GeS}_4\text{Br}_2$. (a) Coordination environments of Pb, Ge, S and Br atoms; (b) the formed 3D Pb–S–Br framework; (c) the isolated $[\text{GeS}_4]$ pseudo-layer structure; and (d) the whole structure of $\text{Pb}_3\text{GeS}_4\text{Br}_2$.

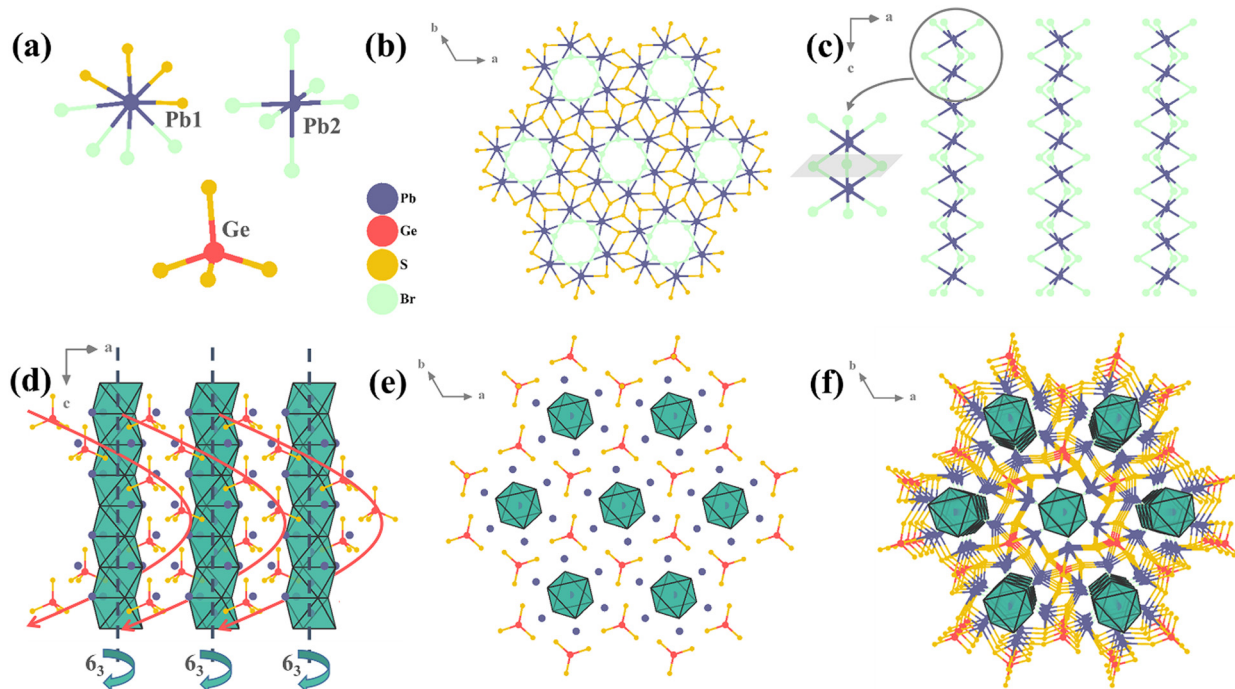


Fig. 2 Crystal structure of $\text{Pb}_{3.5}\text{GeS}_4\text{Br}_3$. (a) Coordination environments of Pb, Ge, S and Br atoms; (b) the $3\text{D } \infty[\text{Pb}_6\text{S}_{21}\text{Br}_{12}]_n$ tunnel-like 3D framework; (c) the $\infty[\text{Pb}_2\text{Br}_3]_n$ column configurations; (d) the isolated $[\text{GeS}_4]$ tetrahedra arranged around the 6_3 axis; (e) The Pb1 atoms and $\infty[\text{Pb}_2\text{Br}_3]_n$ column configurations located within the $[\text{GeS}_4]$ tunnel-like 0D framework; and (f) the whole structure of $\text{Pb}_{3.5}\text{GeS}_4\text{Br}_3$.

ing materials, but it resulted in low yields (the secondary phase is $\text{Pb}_{3.5}\text{GeS}_4\text{Br}_3$, Fig. S4b†). Since $\text{Pb}_{3.5}\text{GeS}_4\text{Br}_3$ crystallizes in the NCS $P6_3$ space group, the NLO response of the compound was evaluated by the Kurtz–Perry method under a $2.09\text{ }\mu\text{m}$ solid-state laser by using the polycrystalline samples. As shown in Fig. 3a, the SHG response of $\text{Pb}_{3.5}\text{GeS}_4\text{Br}_3$ was found to be ~ 0.8 times than that of the benchmark AGS (Fig. S5†), comparable with the value of $0.7 \times \text{AGS}$ in the

recently reported salt-inclusion chalcogenide IR NLO material $\text{Li}[\text{LiCs}_2\text{Cl}][\text{Ga}_3\text{S}_6]$.⁴² Meanwhile, the SHG intensities are increased with particle size augmentation until saturation occurs, indicating that $\text{Pb}_{3.5}\text{GeS}_4\text{Br}_3$ is a PM compound at the $2.09\text{ }\mu\text{m}$ pumping, which is critical for practical applications. Based on statistical analyses (Table 2), and to the best of our knowledge, it is the first thiogermanate halide IR NLO material with PM behavior. To explain the origin of PM in this compound, the RID (usually $\Delta n \geq \text{RID}$) of $\text{Pb}_{3.5}\text{GeS}_4\text{Br}_3$ was investigated, and the measured RID is ~ 0.05 at 546 nm (Fig. S6†). This means that the birefringence Δn of the compound should be larger than 0.05 at 546 nm ,^{23,26,63,64} which is consistent with the PM behavior as shown in Fig. 3a. These results indicate the feasibility for the exploration of PM NLO materials by introducing Pb^{2+} into the structure.

Beyond the NLO response, the band gap is another important parameter for an excellent IR NLO material. To detect the experimental optical band gap, the UV-vis-NIR diffuse reflectance spectrum of $\text{Pb}_{3.5}\text{GeS}_4\text{Br}_3$ was recorded on a SolidSpec-3700 DUV spectrophotometer. The band gap of $\text{Pb}_{3.5}\text{GeS}_4\text{Br}_3$ was found to be $\sim 2.6\text{ eV}$ (Fig. 3b). It is comparable with the band gaps of recently developed Pb-containing chalcogenide IR NLO materials such as $\text{Pb}_2\text{P}_2\text{S}_6$ (2.6 eV),⁶⁵ Pb_4SeBr_6 (2.62 eV),⁶⁶ and $\text{PbGa}_2\text{GeS}_6$ (2.64 eV),⁶⁷ and larger than those of $\alpha\text{-Pb}_2\text{GeSe}_4$ (1.42 eV),⁶⁸ $\text{Sr}_{0.25}\text{Pb}_{1.75}\text{GeSe}_4$ (1.48 eV),⁶⁸ $\text{Sr}_{1.3}\text{Pb}_{0.7}\text{GeSe}_4$ (1.65 eV),⁶⁸ $\text{Pb}_{0.72}\text{Mn}_{2.84}\text{Ga}_{2.95}\text{Se}_8$ (1.65 eV),⁶⁹ $\text{Pb}_2\text{Ga}_4\text{GeSe}_{12}$ (1.91 eV),⁷⁰ $\text{Ag}_2\text{Pb}_3\text{Si}_2\text{S}_8$ (1.95 eV),⁷¹ $\text{PbGa}_2\text{GeSe}_6$ (1.96 eV),⁷² PbSnSiS_4 (2 eV),⁷³ Pb_3SBrI_3 (2.16 eV),⁷⁴

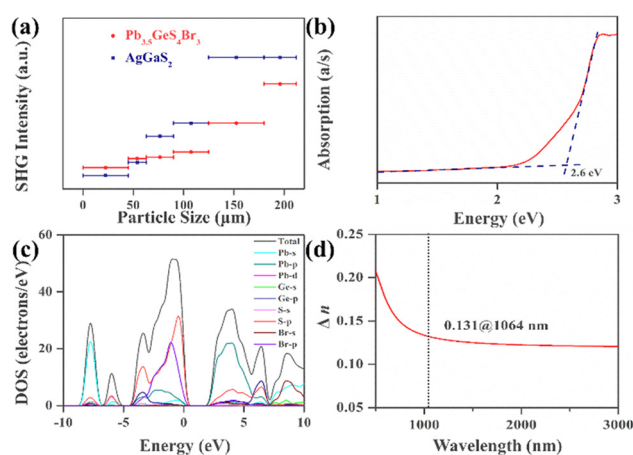


Fig. 3 The SHG intensity versus particle sizes (a) and experimental band gap (b) of $\text{Pb}_{3.5}\text{GeS}_4\text{Br}_3$. The density of states (DOS), partial DOS (c) and the calculated birefringence (d) of $\text{Pb}_3\text{GeS}_4\text{Br}_2$.

Table 2 The space group, band gaps, SHG efficiency PM behavior and Δn (cal) of title compound and typical Ge-containing salt-inclusion chalcogenides NLO materials

| Compounds | Space group | E_g (eV) ^a | SHG efficiency (\times AGS) | PM/NPM ^b | Δn | Ref. |
|--|---------------------------------|-------------------------|--|---------------------|-------------------------------|-----------|
| Pb_{3.5}GeS₄Br₃ | P6₃ (no. 173) | 2.6 | 0.8 (@2090 nm, 180–212 μm) | PM | > 0.05 @ 546 nm | This work |
| [Ba ₄ Cl ₂][Ge ₃ Se ₉] | P6 ₃ (no. 173) | 1.89 | 0.4 (@2050 nm, 30–46 μ m) | NPM | Unknown | 43 |
| [Ba ₄ Cl ₂][Ge ₃ S ₉] | P6 ₃ (no. 173) | 2.91 | 2.4 (@2050 nm, 46–74 μ m) | NPM | 0.019 | 43 |
| [Ba ₄ Br ₂][Ge ₃ Se ₉] | P6 ₃ (no. 173) | 2.6 | 3.5 (@2090 nm, 20–40 μ m) | NPM | 0.028 (@2090 nm) ^c | 44 |
| [NaSr ₄ Cl][Ge ₃ S ₁₀] | P6 ₃ (no. 173) | 3.51 | 0.91 (@2090 nm, 54–100 μ m) | NPM | Unknown | 45 |
| [KSr ₄ Cl][Ge ₃ S ₁₀] | P6 ₃ (no. 173) | 3.54 | 1.08 (@2090 nm, 54–100 μ m) | NPM | Unknown | 45 |
| [KBa ₄ Cl][Ge ₃ S ₁₀] | P6 ₃ (no. 173) | 3.57 | 0.82 (@2090 nm, 54–100 μ m) | NPM | Unknown | 45 |
| [Sr ₄ Cl ₂][Ge ₃ S ₉] | P6 ₃ (no. 173) | 3.71 | 0.97 (@2090 nm, 54–100 μ m) | NPM | 0.005 (@2050 nm) ^c | 46 |
| [NaBa ₄ Cl][Ge ₃ S ₁₀] | P6 ₃ (no. 173) | 3.49 | 0.33 (@2090 nm, 80–100 μ m) | NPM | 0.005 (@2050 nm) ^c | 47 |
| [K ₂ Ba ₃ Cl ₂][Ge ₃ S ₉] | P6 ₃ (no. 173) | 3.69 | 0.34 (@2100 nm, 75–110 μ m) | NPM | 0.032 (@2100 nm) ^c | 48 |

^a Experimental value. ^b PM = phase-matching, NPM = non-phase-matching. ^c Calculated value.

Pb₅Ga₆ZnS₁₅ (2.32 eV),⁷⁵ β -PbGa₂S₄ (2.46 eV),⁷⁶ and Li₂PbSiS₄ (2.51 eV).⁷⁷ Usually, the LIDT is proportional to the band gap, thermal conductivity, and the sample quality. The LIDT of Pb_{3.5}GeS₄Br₃ was found to \sim 3 times than that of AGS. However, for practical applications, obtaining a single crystal of large size is essential. Since Pb_{3.5}GeS₄Br₃ belongs to the chalcogenide group, to increase the single crystal size, the Bridgman–Stockbarger method could be a good choice for the growth of its single crystal. Meanwhile, to improve the crystal-line quality, the crystal growth process should be optimized.

To detect the optical properties of Pb₃GeS₄Br₂, DFT calculations were carried out. The calculated band structure indicates that Pb₃GeS₄Br₂ is an indirect band-gap compound with a theoretical GGA band gap of 2.27 eV (Fig. S7†), which is usually underestimated because the GGA served as an exchange-correlation functional. To ensure the calculated accuracy, the HSE06 method was applied.⁷⁸ The calculated HSE06 band gap is \sim 2.74 eV. From the density of states (DOS) (Fig. 3c), the top of the valence band (VB) is predominately derived from the S-3p and Br-4p orbitals, while the bottom of the conduction band (CB) is occupied by the Pb-6p orbital. This means the band gap of Pb₃GeS₄Br₂ is mainly determined by the [PbS₄Br₄], [PbS₃Br₃] and [PbS₈] units. Since the compound shows evident structural anisotropy, the birefringence of Pb₃GeS₄Br₂ was studied by DFT calculations, and the computed birefringence is \sim 0.131@1064 nm (Fig. 3d), higher than those of other thiogermanate halides like [K₂Ba₃Cl₂][Ge₃S₉] (0.032@2100 nm), [Ba₄Br₂][Ge₃Se₉] (0.028@2090 nm), [Sr₄Cl₂][Ge₃S₉] (0.005@2050 nm), and [NaBa₄Cl][Ge₃S₁₀] (0.005@2050 nm).^{44,46–48} The birefringence of Pb₃GeS₄Br₂ is significantly larger than that of Pb_{3.5}GeS₄Br₃, because of the evident SCALP electrons of Pb²⁺ in the compound.

Conclusions

In conclusion, by introducing the Pb²⁺ cation into thiogermanate halides, the first series of Pb-containing thiogermanate halides, Pb₃GeS₄Br₂ and Pb_{3.5}GeS₄Br₃, were successfully synthesized. The compounds show distinctive crystal structures. Compared to the Pb₃GeS₄Br₂, the higher Pb and Br ratios give

rise to a columnar configuration along the 6₃ spiral axis direction of the structure in Pb_{3.5}GeS₄Br₃, resulting in a better arrangement of tetrahedral motifs and higher symmetry in the compound. More importantly, Pb_{3.5}GeS₄Br₃ exhibits a large SHG response (0.8 \times AGS) with PM behaviour and a high LIDT (3 \times AGS). Meanwhile, Pb₃GeS₄Br₂, containing Pb²⁺ with SCALP electrons, shows a large birefringence of \sim 0.131@1064 nm, indicating that the Pb²⁺ cation with SCALP electrons can effectively enhance the birefringence of thiogermanate halides.

Author contributions

Xiangzhan Jiang, Jiale Qu and Yu Chu designed and guided the experiments and wrote the manuscript. Jiazheng Zhou synthesized the samples, characterized the properties, and wrote the manuscript. Hongshan Wang, Junjie Liu and Xin Su carried out the DFT calculations.

Conflicts of interest

The authors declare no conflict of interest.

Acknowledgements

This work was supported by the National Natural Science Foundation of China (61835014 and 51972336), the Xinjiang Tianshan Talent Program (2022TSYCTD0005), and the Scientific Foundation of Binzhou Medical University (No. 50012304488).

References

- 1 P. F. Li, C. L. Hu, B. X. Li, J. G. Mao and F. Kong, From CdPb₈(SeO₃)₄Br₁₀ to Pb₃(TeO₃)Br₄: the first tellurite bromide exhibiting an SHG response and mid-IR transparency, *Inorg. Chem. Front.*, 2023, **10**, 7343–7350.

2 M. S. Zhang, B. W. Liu, X. M. Jiang and G. C. Guo, $\text{AlIn}_3\text{Si}_4\text{P}_9$ (A = Ca, Sr): Quaternary phosphides with double-helix structures exhibiting high laser-induced damage thresholds, *Inorg. Chem. Front.*, 2023, **10**, 1112–1118.

3 C. Yang, X. Liu, C. L. Teng, X. H. Cheng, F. Liang and Q. Wu, Hierarchical molecular design of high-performance infrared nonlinear Ag_2HgI_4 material by defect engineering strategy, *Mater. Today Phys.*, 2021, **19**, 100432–100439.

4 L. Luo, L. A. Wang, J. B. Chen, J. Z. Zhou, Z. H. Yang, S. L. Pan and J. J. Li, $\text{AlB}_3\text{IIC}_3\text{IIIQ}_8\text{VI}$: A new family for the design of infrared nonlinear optical materials by coupling octahedra and tetrahedra units, *J. Am. Chem. Soc.*, 2022, **144**, 21916–21925.

5 M. Mutailipu, M. Zhang, H. P. Wu, Z. H. Yang, Y. H. Shen, J. L. Sun and S. L. Pan, $\text{Ba}_3\text{Mg}_3(\text{BO}_3)_3\text{F}_3$ polymorphs with reversible phase transition and high performances as ultraviolet nonlinear optical materials, *Nat. Commun.*, 2018, **9**, 3089.

6 S. X. Cui, H. P. Wu, X. K. Dong, Z. G. Hu, J. Y. Wang, Y. C. Wu, K. R. Poeppelmeier and H. W. Yu, Chiral and, polar duality design of heteroanionic compounds: $\text{Sr}_{18}\text{Ge}_9\text{O}_5\text{S}_{31}$ based on $\text{Sr}_3\text{OGeS}_3^{2+}$ and $\text{Sr}_3\text{SGeS}_3^{2+}$ groups, *Adv. Sci.*, 2023, **11**, 2306825.

7 C. T. Chen, B. C. Wu, A. D. Jiang and G. M. You, A new-type ultraviolet SHG crystal: Beta- BaB_2O_4 , *Sci. Sin., Ser. B*, 1985, **28**, 235–243.

8 C. T. Chen, Y. C. Wu, A. D. Jiang, B. C. Wu, G. M. You, R. K. Li and S. J. Lin, New nonlinear-optical crystal: LiB_3O_5 , *J. Opt. Soc. Am. B*, 1989, **6**, 616–621.

9 J. West, A quantitative X-ray analysis of the structure of potassium dihydrogen phosphate (KH_2PO_4), *Z. Kristallogr.*, 1930, **74**, 306–332.

10 Y. S. Liu, L. Drafall, D. Dentz and R. Belt, Non-linear optical-properties of KTiOPO_4 (KTP), *IEEE J. Quantum Electron.*, 1981, **17**, 26–26.

11 J. J. Li and F. L. Deepak, In situ kinetic observations on crystal nucleation and growth, *Chem. Rev.*, 2022, **122**, 16911–16982.

12 L. Mei, X. Huang, Y. Wang, Q. Wu, B. Wu and C. T. Chen, Crystal Structure of $\text{KBe}_2\text{BO}_3\text{F}_2$, *Z. Kristallogr.*, 1995, **210**, 93–95.

13 G. Q. Shi, Y. Wang, F. F. Zhan, B. B. Zhang, Z. H. Yang, X. L. Hou, S. L. Pan and K. R. Poeppelmeier, Finding the next deep-ultraviolet nonlinear optical material: $\text{NH}_4\text{B}_4\text{O}_6\text{F}$, *J. Am. Chem. Soc.*, 2017, **139**, 10645–10648.

14 Y. C. Qin, M. D. Zhu, Y. Tang, X. Q. Chen, F. Wang and X. Y. Fan, Strong alternating piezoelectric field enhanced the piezocatalytic degradation of carbamazepine by a 3-chromophore material $\text{Cd}_4\text{BiO}(\text{BO}_3)_3$ coupled ultrasound in water, *Chem. Eng. J.*, 2023, **469**, 143911.

15 X. F. Wang, Y. Wang, B. B. Zhang, F. F. Zhang, Z. H. Yang and S. L. Pan, $\text{CsB}_4\text{O}_6\text{F}$: A congruent-melting deep-ultraviolet nonlinear optical material by combining superior functional units, *Angew. Chem., Int. Ed.*, 2017, **56**, 14119–14123.

16 M. Mutailipu, M. Zhang, B. B. Zhang, L. Y. Wang, Z. H. Yang, X. Zhou and S. L. Pan, $\text{SrB}_5\text{O}_7\text{F}_3$ functionalized with $[\text{B}_5\text{O}_9\text{F}_3]^{6-}$ chromophores: accelerating the rational design of deep-ultraviolet nonlinear optical materials, *Angew. Chem., Int. Ed.*, 2018, **57**, 6095–6099.

17 B. B. Zhang, G. Q. Shi, Z. H. Yang, F. F. Zhang and S. L. Pan, Fluorooxoborates: beryllium-free deep-ultraviolet nonlinear optical materials without layered growth, *Angew. Chem., Int. Ed.*, 2017, **56**, 3916–3919.

18 P. Wang, Y. Chu, A. Tudi, C. W. Xie, Z. H. Yang, S. L. Pan and J. J. Li, The combination of structure prediction and experiment for the exploration of alkali-earth metal-contained chalcopyrite-like IR nonlinear optical material, *Adv. Sci.*, 2022, **9**, e2106120.

19 B. Tell and H. M. Kasper, Optical and, electrical properties of AgGaS_2 and AgGaSe_2 , *Phys. Rev. B: Solid State*, 1971, **4**, 4455–4459.

20 G. D. Boyd, E. Buehler and F. G. Storz, Linear and, non-linear optical properties of ZnGeP_2 and CdSe , *Appl. Phys. Lett.*, 1971, **18**, 301–304.

21 S. Yang, C. Lin, H. Fan, K. Chen, G. Zhang, N. Ye and M. Luo, Polar phosphorus chalcogenide cage molecules: Enhancement of nonlinear optical properties in adducts, *Angew. Chem., Int. Ed.*, 2023, **62**, e202218272.

22 L. A. Wang, Q. Sun and J. J. Li, Recent progress on sulfide infrared nonlinear optical materials with large SHG response and wide band gap, *Chin. J. Struct. Chem.*, 2023, **42**, 100013.

23 J. Z. Zhou, Z. X. Fan, K. W. Zhang, Z. H. Yang, S. L. Pan and J. J. Li, $\text{Rb}_2\text{CdSi}_4\text{S}_{10}$: novel $[\text{Si}_4\text{S}_{10}]$ T2-supertetrahedra-contained infrared nonlinear optical material with large band gap, *Mater. Horiz.*, 2023, **10**, 619–624.

24 H. T. Qiu, F. M. Li, C. C. Jin, Z. H. Yang, J. J. Li, S. L. Pan and M. Mutailipu, Fluorination strategy towards symmetry breaking of boron-centered tetrahedron for poly-fluorinated optical crystals, *Angew. Chem., Int. Ed.*, 2023, **63**, e202316194.

25 Y. Chu, H. S. Wang, T. Abutukadi, Z. Li, M. Mutailipu, X. Su, Z. H. Yang, J. J. Li and S. L. Pan, $\text{Zn}_2\text{HgP}_2\text{S}_8$: A wide bandgap hg-based infrared nonlinear optical material with large second-harmonic generation response, *Small*, 2023, **19**, 2305074.

26 A. Abudurusuli, J. B. Huang, P. Wang, Z. H. Yang, S. L. Pan and J. J. Li, $\text{Li}_4\text{MgGe}_2\text{S}_7$: The first alkali and alkaline-earth diamond-like infrared nonlinear optical material with exceptional large band gap, *Angew. Chem., Int. Ed.*, 2021, **60**, 24131–24136.

27 J. Xu, K. Wu, B. Zhang, H. Yu and H. Zhang, $\text{LaAeAl}_3\text{S}_7$ (Ae = Ca, Sr): Cairo pentagonal layered thioaluminates achieving a good balance between a strong second harmonic generation response and a wide bandgap, *Inorg. Chem. Front.*, 2023, **10**, 2045–2052.

28 Y. J. Zhang, H. P. Wu, Z. G. Hu, J. Y. Wang, Y. C. Wu and H. W. Yu, Achieving a strong second harmonic generation response and a wide band gap in a Hg-based material, *Inorg. Chem. Front.*, 2022, **9**, 4075–4080.

29 Y. Chu, H. S. Wang, Q. Chen, X. Su, Z. X. Chen, Z. H. Yang, J. J. Li and S. L. Pan, "Three-in-One": A new Hg-based selenide $\text{Hg}_2\text{P}_2\text{Se}_{12}$ exhibiting wide infrared transparency range and strong nonlinear optical effect, *Adv. Funct. Mater.*, 2023, DOI: [10.1002/adfm.202314933](https://doi.org/10.1002/adfm.202314933).

30 L. Wang, D. Chu, D. Yin, C. Xie, Z. Yang, J. Li and S. Pan, Theoretical investigations on ternary defective diamond-like infrared nonlinear optical materials in Be-Ga-Se system, *Mater. Today Phys.*, 2023, **38**, 101245.

31 J. J. Li, J. C. Chen, H. Wang, N. Chen, Z. C. Wang, L. Guo and F. L. Deepak, In situ atomic-scale study of particle-mediated nucleation and growth in amorphous bismuth to nanocrystal phase transformation, *Adv. Sci.*, 2018, **5**, 1700992.

32 J. J. Li, Z. C. Wang and F. L. Deepak, In situ atomic-scale observation of droplet coalescence driven nucleation and growth at liquid/solid interfaces, *ACS Nano*, 2017, **11**, 5590–5597.

33 H. S. Wang, Y. Chu, X. T. Pan, Z. H. Yang, S. L. Pan and J. J. Li, Double alkaline earth metals sulfide SrMgGeS_4 with high laser-induced damage threshold and strong second-harmonic generation, *Mater. Today Phys.*, 2023, **38**, 101243.

34 S. M. Pei, B. W. Liu, W. F. Chen, X. M. Jiang and G. C. Guo, Breaking the bottleneck of simultaneously wide band gap and large nonlinear optical coefficient by a "pore reconstruction" strategy in a salt-inclusion chalcogenide, *Mater. Horiz.*, 2023, **10**, 2921–2926.

35 J. Z. Zhou, L. A. Wang, Y. Chu, H. S. Wang, S. L. Pan and J. J. Li, $\text{Na}_3\text{SiS}_3\text{F}$: A wide bandgap fluorothiosilicate with unique SiS_3F unit and high laser-induced damage threshold, *Adv. Opt. Mater.*, 2023, **11**, 2300736.

36 L. A. Wang, C. C. Tu, H. B. Gao, J. Z. Zhou, H. S. Wang, Z. H. Yang, S. L. Pan and J. J. Li, Clamping effect driven design and fabrication of new infrared birefringent materials with large optical anisotropy, *Sci. China: Chem.*, 2023, **66**, 1086–1093.

37 X. Y. Lou, X. M. Jiang, B. W. Liu and G. C. Guo, Excellent nonlinear optical $\text{M}[\text{M}_4\text{Cl}][\text{Ga}_{11}\text{S}_{20}]$ ($\text{M} = \text{A/Ba, A = K, Rb}$) achieved by unusual cationic substitution strategy, *Small*, 2023, **20**, 2305711.

38 H. Chen, Y. Y. Li, B. X. Li, P. F. Liu, H. Lin, Q. L. Zhu and X. T. Wu, Salt-inclusion chalcogenide $[\text{Ba}_4\text{Cl}_2][\text{ZnGa}_4\text{S}_{10}]$: rational design of an IR nonlinear optical material with superior comprehensive performance derived from AgGaS_2 , *Chem. Mater.*, 2020, **32**, 8012–8019.

39 L. A. Wang, C. C. Tu, J. Z. Zhou, Y. Chu, Z. H. Yang, S. L. Pan and J. J. Li, Mixed anionic tetrahedra guided design of new infrared nonlinear optical material $\text{Cs}_3\text{Ga}_8\text{S}_{13}\text{Cl}$ with high laser-induced damage threshold, *Adv. Opt. Mater.*, 2023, **12**, 2301634.

40 K. X. Ding, H. P. Wu, Z. G. Hu, J. Y. Wang, Y. C. Wu and H. W. Yu, $\text{Ba}_4(\text{S}_2)\text{ZnGa}_4\text{S}_{10}$: design of an unprecedented infrared nonlinear salt-inclusion chalcogenide with disulfide-bonds, *Small*, 2023, **19**, 2302819.

41 C. Y. Zhao, K. Wu, Y. Xiao, B. B. Zhang, H. H. Yu and H. J. Zhang, $[\text{Sr}_4\text{Cl}_2][\text{Si}_3\text{S}_9]$: Ultrawide-bandgap salt-inclusion thiosilicate nonlinear optical material with unprecedented tri-polymerized $[\text{Si}_3\text{S}_9]$ clusters, *J. Mater. Chem. C*, 2023, **11**, 4439–4443.

42 B. W. Liu, X. M. Jiang, B. X. Li, H. Y. Zeng and G. C. Guo, $[\text{LiCs}_2\text{Cl}][\text{Ga}_3\text{S}_6]$: Unprecedented tetrahedra-built nanoporous framework with excellent nonlinear optical performance, *Angew. Chem., Int. Ed.*, 2019, **59**, 4856–4859.

43 P. F. Liu, Y. Y. Li, Y. J. Zheng, J. S. Yu, R. H. Duan, H. Chen, H. Lin, L. Chen and L. M. Wu, Tailored synthesis of nonlinear optical quaternary chalcogenides: $\text{Ba}_4\text{Ge}_3\text{S}_9\text{Cl}_2$, $\text{Ba}_4\text{Si}_3\text{Se}_9\text{Cl}_2$ and $\text{Ba}_4\text{Ge}_3\text{Se}_9\text{Cl}_2$, *Dalton Trans.*, 2017, **46**, 2715–2721.

44 W. H. Xing, N. Z. Wang, A. K. Iyer, W. L. Yin, Z. S. Lin, J. Y. Yao, B. Kang and A. Mar, Evaluation of nonlinear optical properties of quaternary chalcogenide halides $\text{Ba}_4\text{Si}_3\text{Se}_9\text{Br}_2$ and $\text{Ba}_4\text{Ge}_3\text{Se}_9\text{Br}_2$, *J. Alloys Compd.*, 2020, **846**, 156398–156468.

45 Y. Song, S. Cui, Z. Qian, H. Yu, Z. Hu, J. Wang, Y. Wu and H. Wu, $[\text{ASr}_4\text{Cl}][\text{Ge}_3\text{S}_{10}]$ ($\text{A} = \text{Na, K}$) and $[\text{KBa}_4\text{Cl}][\text{Ge}_3\text{S}_{10}]$: new salt-inclusion infrared nonlinear optical crystals with zero-dimensional $[\text{Ge}_3\text{S}_9]$ clusters, *Inorg. Chem. Front.*, 2022, **9**, 5932–5940.

46 Y. F. Song, Z. Qian, B. R. Zhou, H. W. Yu, Z. G. Hu, J. Y. Wang, Y. C. Wu and H. P. Wu, A non-centrosymmetric chalcogenide synthesized through the combination of chemical tailoring with aliovalent substitution, *Chem. Commun.*, 2023, **59**, 3309–3312.

47 K. Feng, L. Kang, Z. S. Lin, J. Y. Yao and Y. C. Wu, Noncentrosymmetric chalcogenide $\text{NaBa}_4\text{Ge}_3\text{S}_{10}\text{Cl}$ with large band gap and IR NLO response, *J. Mater. Chem. C*, 2014, **2**, 4590–4596.

48 W. Zhou, Z.-H. Shi, W. Liu and S.-P. Guo, Noncentrosymmetric chalcogenide $\text{K}_2\text{Ba}_3\text{Ge}_3\text{S}_9\text{Cl}_2$: A new nonlinear optical material with remarkable laser-induced damage threshold, *J. Alloys Compd.*, 2022, **895**, 162602.

49 J. Guo, A. Tudi, S. Han, Z. Yang and S. Pan, $\alpha\text{-SnF}_2$: A UV birefringent material with large birefringence and easy crystal growth, *Angew. Chem., Int. Ed.*, 2021, **60**, 3540–3544.

50 L. Haeming and G. M. Sheldrick, SADABS: A program for exploiting the redundancy of area-detector X-RAY data, *Acta Crystallogr., Sect. A: Found. Crystallogr.*, 1999, **55**, 206–206.

51 G. M. Sheldrick, A short history of SHELX, *Acta Crystallogr., Sect. A: Found. Crystallogr.*, 2008, **64**, 112–122.

52 A. L. Spek, Single-crystal structure validation with the program PLATON, *J. Appl. Crystallogr.*, 2003, **36**, 7–13.

53 J. Tauc, Absorption edge and, internal electric fields in amorphous semiconductors, *Mater. Res. Bull.*, 1970, **5**, 721–729.

54 S. J. Clark, M. D. Segall, C. J. Pickard, P. J. Hasnip, M. J. Probert, K. Refson and M. C. Payne, First principles methods using CASTEP, *Z. Kristallogr.*, 2005, **220**, 567–570.

55 J. P. Perdew, K. Burke and M. Ernzerhof, Generalized gradient approximation made simple, *Phys. Rev. Lett.*, 1996, **77**, 3865–3868.

56 X. F. Wang, J. J. Li, Z. J. Zhao, S. M. Huang and W. H. Xie, Crystal structure and electronic structure of quaternary

semiconductors $\text{Cu}_2\text{ZnTiSe}_4$ and $\text{Cu}_2\text{ZnTiS}_4$ for solar cell absorber, *J. Appl. Phys.*, 2012, **112**, 023701.

57 A. M. Rappe, K. M. Rabe, E. Kaxiras and J. D. Joannopoulos, Optimized pseudopotentials, *Phys. Rev. B: Condens. Matter Mater. Phys.*, 1990, **41**, 1227–1230.

58 J. Heyd, J. E. Peralta, G. E. Scuseria and R. L. Martin, Energy band gaps and lattice parameters evaluated with the Heyd-Scuseria-Ernzerhof screened hybrid functional, *J. Chem. Phys.*, 2005, **123**, 224106.

59 S. K. Kurtz and T. T. Perry, A powder technique for the evaluation of nonlinear optical materials, *J. Appl. Phys.*, 1968, **39**, 3798–3813.

60 H. Wang, X. Pan, W. Zhao, Y. Chu and J. Li, A new infrared nonlinear optical material BaZnGeS_4 with a wide band gap and large nonlinear optical response, *Inorg. Chem. Front.*, 2023, **10**, 6253–6261.

61 J.-H. Cha, J. H. Han, W. Yin, C. Park, Y. Park, T. K. Ahn, J. H. Cho and D.-Y. Jung, Photoresponse of CsPbBr_3 and Cs_4PbBr_6 perovskite single crystals, *J. Phys. Chem. Lett.*, 2017, **8**, 565–570.

62 A. V. Baranov, K. V. Bogdanov, E. V. Ushakova, S. A. Cherevkov, A. V. Fedorov and S. Tscharntke, Comparative analysis of Raman spectra of PbS macro- and nanocrystals, *Opt. Spectrosc.*, 2010, **109**, 268–271.

63 C. Jiang, X. Jiang, C. Wu, Z. Huang, Z. Lin, M. G. Humphrey and C. Zhang, Isoreticular Design of KTiOPO_4 -Like Deep-Ultraviolet Transparent Materials Exhibiting Strong Second-Harmonic Generation, *J. Am. Chem. Soc.*, 2022, **144**, 20394–20399.

64 S. S. Shi, C. S. Lin, G. S. Yang, L. L. Cao, B. X. Li, T. Yan, M. Luo and N. Ye, $\text{A}_2\text{Bi}_2(\text{SeO}_3)_3\text{F}_2$ ($\text{A} = \text{K}$ and Rb): Excellent Mid-Infrared Nonlinear Optical Materials with Both Strong SHG Responses and Large Band Gaps, *Chem. Mater.*, 2020, 7958–7964.

65 B. Ji, A. Sarkar, K. Wu, A. Swindle and J. Wang, $\text{A}_2\text{P}_2\text{S}_6$ ($\text{A} = \text{Ba}$ and Pb): a good platform to study the polymorph effect and lone pair effect to form an acentric structure, *Dalton Trans.*, 2022, **51**, 4522–4531.

66 J. K. Wang, H. P. Wu, H. W. Yu, Z. G. Hu, J. Y. Wang and Y. C. Wu, Pb_4SeBr_6 : A congruently melting mid-infrared nonlinear optical material with excellent comprehensive performance, *Adv. Opt. Mater.*, 2022, **10**, 2102673.

67 Y.-Z. Huang, H. Zhang, C.-S. Lin, W.-D. Cheng, Z. Guo and G.-L. Chai, $\text{PbGa}_2\text{GeS}_6$: An infrared nonlinear optical material synthesized by an intermediate-temperature self-fluxing method, *Cryst. Growth Des.*, 2018, **18**, 1162–1167.

68 L. T. Menezes, A. Assoud, W. Zhang, P. S. Halasyamani and H. Kleinke, Effect of Pb substitution in $\text{Sr}_{2-x}\text{Pb}_x\text{GeSe}_4$ on crystal structures and nonlinear optical properties predicted by DFT calculations, *Inorg. Chem.*, 2020, **59**, 15028–15035.

69 M. L. Zhou, X. X. Jiang, Y. W. Guo, Z. S. Lin, J. Y. Yao and Y. C. Wu, $\text{Pb}_{0.65}\text{Mn}_{2.85}\text{Ga}_3\text{S}_8$ and $\text{Pb}_{0.72}\text{Mn}_{2.84}\text{Ga}_{2.95}\text{Se}_8$: two quaternary metal chalcognides with open-tunnel-framework structures displaying intense second harmonic generation responses and interesting magnetic properties, *Inorg. Chem.*, 2017, **56**, 8454–8461.

70 Y. K. Chen, M. C. Chen, L. J. Zhou, L. Chen and L. M. Wu, Syntheses, structures, and nonlinear optical properties of quaternary chalcogenides: $\text{Pb}_4\text{Ga}_4\text{GeQ}_{12}$ ($\text{Q} = \text{S, Se}$), *Inorg. Chem.*, 2013, **52**, 8334–8341.

71 G. C. M. Wessler, T. L. Wang, V. Blum and D. B. Mitzi, Cubic crystal structure formation and optical properties within the $\text{Ag}-\text{B}^{\text{II}}-\text{M}^{\text{IV}}-\text{X}$ ($\text{B}^{\text{II}} = \text{Sr, Pb}$, $\text{M}^{\text{IV}} = \text{Si, Ge, Sn}$; $\text{X} = \text{S, Se}$) family of semiconductors, *Inorg. Chem.*, 2022, **61**, 2929–2944.

72 V. V. Badikov, D. V. Badikov, L. Wang, G. S. Shevyrdyaeva, V. L. Panyutin, A. A. Fintisova, S. G. Sheina and V. Petrov, Crystal growth and, characterization of a new quaternary chalcogenide nonlinear crystal for the mid-infrared: $\text{PbGa}_2\text{GeSe}_6$, *Cryst. Growth Des.*, 2019, **19**, 4224–4228.

73 J. Z. Zhou, L. Luo, Y. Chu, P. Wang, Z. Y. Guo, X. Su and J. J. Li, Partial congener substitution induced centrosymmetric to noncentrosymmetric structural transformation and nonlinear optical properties of PbSnSiS_4 , *J. Alloys Compd.*, 2022, **899**, 163366.

74 M. Yan, R. L. Tang, W. Zhou, W. Liu and S. P. Guo, Pb_3SBrI_3 : the first Pb-based chalcohalide with multiple halogens features a unique two-dimensional structure composed of diverse Pb-centered polyhedra, *Dalton Trans.*, 2022, **51**, 12921–12927.

75 R. H. Duan, J. S. Yu, H. Lin, Y. J. Zheng, H. J. Zhao, S. X. Huang-Fu, M. A. Khan, L. Chen and L. M. Wu, $\text{Pb}_5\text{Ga}_6\text{ZnS}_{15}$: a noncentrosymmetric framework with chains of T2-supertetrahedra, *Dalton Trans.*, 2016, **45**, 12288–12291.

76 W. F. Chen, B. W. Liu, X. M. Jiang and G. C. Guo, Infrared nonlinear optical performances of a new sulfide $\beta\text{-PbGa}_2\text{S}_4$, *J. Alloys Compd.*, 2022, **905**, 164090.

77 Z. Akil, H. Boutaleb, M. Zemouli, M. Keteb, K. Amara and M. Elkeurti, Enhancing second harmonic generation response in infrared nonlinear optical material through Pb substitution: a study of $\text{Li}_2\text{PbSiS}_4$ compound, *Optik*, 2023, **294**, 171441.

78 Y. Wang, B. B. Zhang, Z. H. Yang and S. L. Pan, Cation-tuned synthesis of fluorooxoborates: Towards optimal deep-ultraviolet nonlinear optical materials, *Angew. Chem., Int. Ed.*, 2018, **57**, 2150–2154.